Supporting Information for

Investigation and control of metallogel formation for the deposition of supramolecular nanotubes of single-chain magnets

Felix Houard,[a] Andrea Olivier,[a] Giuseppe Cucinotta,[b] Olivier Galangau,[a] Marie Gautier,[d] Franck Camerel,[a] Thierry Guizouarn,[a] Thierry Roisnel,[a] Boris Le Guennic,[a] Mykhaylo Ozerov,[c] Yan Suffren,[a] Guillaume Calvez,[a] Carole Daiguebonne,[a] Olivier Guillou,[a] Franck Artzner,[d] Matteo Mannini,[b]* Kevin Bernot[a,e]*

[a.] *Univ Rennes, INSA Rennes, CNRS, ISCR (Institut des Sciences Chimiques de Rennes), UMR 6226, Université de Rennes 1, Rennes, FRANCE.*

[b.] *Dipartimento di Chimica "Ugo Schiff" (DICUS), Università degli Studi di Firenze, INSTM Research Unit of Firenze, Sesto Fiorentino, ITALY.*

[c.] *National High Magnetic Field Laboratory, Florida State University, Tallahassee, FL, 32310, USA.*

[d.] *CNRS, IPR (Institut de Physique de Rennes), UMR 6251, Université de Rennes, Rennes, FRANCE.*

[e.] *Institut Universitaire de France, Paris, FRANCE.*

Materials

Analytical grade solvents and 4-decyloxybenzaldehyde (TCI Chemicals) were commercially available and used without further purification.

Instruments and methods

Single crystal X-ray diffraction

Fresh single crystals were mounted on a Bruker D8 Venture. Crystal data collection was performed with Mo(K$_\alpha$) radiation (λ = 0.7071 Å). Crystal structure was solved using SHELXT[1] and refined with SHELXL[2] via the WINGX program.[3] Unless explicitly indicated, all non-hydrogen atoms were refined anisotropically and hydrogen atoms located at ideal positions.

Supplementary crystallographic data can be obtained free of charge from the Cambridge Crystallographic Data Centre (CDCC) under the deposition numbers CCDC-2298965 (**NITPhOC10**), CCDC-2298968 (**[Tb(hfac)₃(NITPhOC6)₂]**), CCDC-2298966 (**[Tb(hfac)₃(NITPhOC10)₂]**) and CCDC-2298967 (**[Tb(hfac)₃(NITPhOC18)₂]**).

Powder X-ray diffraction

Experimental diffraction patterns have been collected with a Panalytical X'Pert Pro diffractometer, equipped with an X'Celerator detector. Typical recording conditions were 45 kV, 40 mA for Cu(K$_\alpha$) (λ = 1.541 Å) in θ/θ mode.

Gelation inversion test and determination of the pseudo-phase diagram

Gelation properties were evaluated by introducing a precise amount of the targeted compound and a volume of solvent needed to reach the required weight concentration. The vial was closed and heated with a heat gun until complete dissolution of the compound and homogenization of the solution. The solution was then cooled at targeted temperature with a fixed thermal ramp thanks to a Peltier-based temperature controller qX2/PE1050 (Quantum Northwest, Inc), depending on the gelling dynamics of the compound and the concentration. The effective gelation of the sample was tested by inverting the vial after 5min of thermalization at the considered temperature: if the gel does not flow after one minute, then the test is positive.

Fourier Transformed Infra-Red spectroscopy

FT-IR studies were performed with a Perkin Elmer Frontier UATR spectrometer on as-synthesized powders, gels and precursors (from 4000 to 650 cm⁻¹, resolution 1 cm⁻¹).

Variable temperature UV-Visible spectroscopy

UV-Visible absorption spectra of solutions and gels were recorded on Flame-S spectrophotometer (Ocean Insight) coupled to a DH 2000 Bal lamp in 1 mm Hellma 110-QS cuvettes, in a Peltier-based temperature controller qpod 3 (Quantum Northwest, Inc).

Elemental analyses

Elemental analyses (CHNS) were realized with a Thermo Fischer FlashEA 1112 analyzer.

Rheological measurements

Rheological measurements were carried out using a controlled-stress rheometer (Discovery HR 2, TA Instruments, France) equipped with a Peltier plate to control the temperature and a cone plate geometry. The diameter of the cone plate is 60 mm for an angle of 0.5 ° and a truncation gap of 14 μm. A solvent trap was used during the experiments to prevent solvent evaporation. The temperature of the Peltier plate was set at 10 °C for 20 minutes before the beginning of sample testing. Amplitude sweep tests were conducted at 1 Hz with an oscillation strain amplitude range between 0.01 % and 50 %.

Dynamical Scanning Calorimetry measurements

Differential scanning calorimetry was carried out by using NETZSCH DSC 200 F3 instrument equipped with an intracooler. DSC traces were measured at 0.1, 1 and 10 °C/min from 60 °C down to 4 °C.

Liquid and solid states luminescence measurements

Emission spectra were measured using a Horiba-Jobin Yvon Fluorolog-III spectrofluorimeter, equipped with a three-slit double grating excitation and emission monochromator with dispersions of 2.1 nm·mm^{-1} (1200 grooves·mm^{-1}). The steady-state luminescence was excited by unpolarized light from a 450 W Xenon CW lamp and detected at a 90° angle for solid-state measurement by a red-sensitive Hamamatsu R928 photomultiplier tube (sensitivity 190 - 860 nm). Spectra were corrected for both the excitation source light intensity variation (lamp and grating) and the emission spectral response (detector and grating). Appropriate filters were used to remove the residual excitation laser light, Rayleigh scattered light and associated harmonics from spectra. The excitation/emission spectra recordings were realized on samples placed directly into quartz cuvette and cooled in an optical cryostat capable of reaching temperature down to 77 K through a continuous nitrogen liquid flow and a nitrogen atmosphere inside the sample chamber (OptistatCF, Oxford Inst.).

Electron Spin Resonance (ESR) spectroscopy

Fresh solution and gel samples were prepared inside quartz tubes. ESR spectra were recorded on a Bruker EMX–8/2.7 (X–band) spectrometer at room temperature.

Small Angle X-ray Scattering (SAXS)

Fresh gel samples were prepared inside quartz capillaries. SAXS experiments were performed at room temperature with a home-made setup, using X-ray patterns collected with a Pilatus 300K (Dectris, Grenoble, France) mounted on a GeniX 3D (Xenocs, Sassenage, France) microsource X-ray generator operating at 30 W with a monochromatic Cu(K$_\alpha$) radiation (λ = 1.541 Å).[4] The sample-to-detector distance is 270 mm, and the diffraction patterns were recorded for reciprocal spacing $q = 4\pi \times \sin(\theta)/\lambda$ in a range of repetitive distances from 0.01 Å^{-1} (600 Å) to 1.77 Å^{-1} (8 Å). Images were transformed into graphics using a home-developed program.

Magnetic studies

Magnetic studies were performed using an MPMS SQUID magnetometer equipped with an RSO probe and a ^{3}He insert for hysteresis measurements below 1.5 K (field sweep rate was 15.5 Oe·s^{-1}). Ground powders of **TbCn precursors** were pressed into pellets to avoid in-field crystallite orientation. Fresh gels were transferred in gelatin capsules and quickly frozen at 100 K (the freezing point of the *n-*

heptane being 182 K) to avoid further degradations. Powder measurements were corrected from diamagnetic contributions as calculated with Pascal's constants, and the gel ones by subtracting the diamagnetic contributions of the capsule and solvent measured in the same conditions.

Far-Infrared Magnetospectroscopy studies
Broadband IR measurements were performed in the Voigt transmission configuration using a Bruker 80v Fourier-transform IR spectrometer. The incident IR light from a globar source was guided to the top of the probe inside an evacuated beamline and then delivered to the bottom of the probe through brass light pipes. The sample was in the middle of two confocal 90° off-axis parabolic mirrors mounted at the bottom of the probe. While the first mirror focuses the IR radiation on the sample, the second mirror collimates the radiation to the short light pipe with a 4K composite Si bolometer at the end. The mixture of ~ 3 mg of the powder sample and eicosane was secured with thin polypropylene adhesive film and mounted on the brass plate with a clear aperture of 3 mm. The sample was placed at the centre of a 17.5 T vertical bore superconducting magnet in a helium exchange gas environment, providing the sample temperature of about 5.5 K. IR transmission spectra were collected for 3 min at a fixed magnetic field, changing with 1 T step. All spectra obtained at different magnetic fields were normalized to the same reference spectrum, which is their mean, computed after removing the outlier points at each frequency. Such normalization flattens those spectral features independent of magnetic fields (like phonons and instrument artifacts) and highlights those absorption peaks that shift as the magnetic field increases.

Atomic Force Microscopy (AFM) studies
AFM studies were performed on cleaned silicon substrates (Si <100>, n-doped, 2-5 $\Omega \cdot$cm, Virginia Semiconductors) on which 10 μL of hot solutions were dropped and spin-coated at 2000rpm for 60s. Fresh samples then were kept at 4°C for 2 min, dried under a dry N_2 flux for 15 seconds and mounted on the AFM sample holder. Samples were measured in semicontact mode at room temperature under a gentle nitrogen flux to avoid deterioration of the soft film, with an SPM Solver P47 Pro (NT-MDT Spectrum Instrument) and HQ:NSC36/Al BS silicon tips (cantilever B, 130 kHz, 2 N·m^{-1}, MikroMasch). Results and imaging were processed with Gwyddion v2.56 software,[5] raw images have been treated with a horizontal line-by-line subtraction using a "median of differences" routine in order to fix the line scan misalignment issue.

Synthesis and gelation properties

Synthesis of the nitronyl-nitroxide radical, NITPhOC10
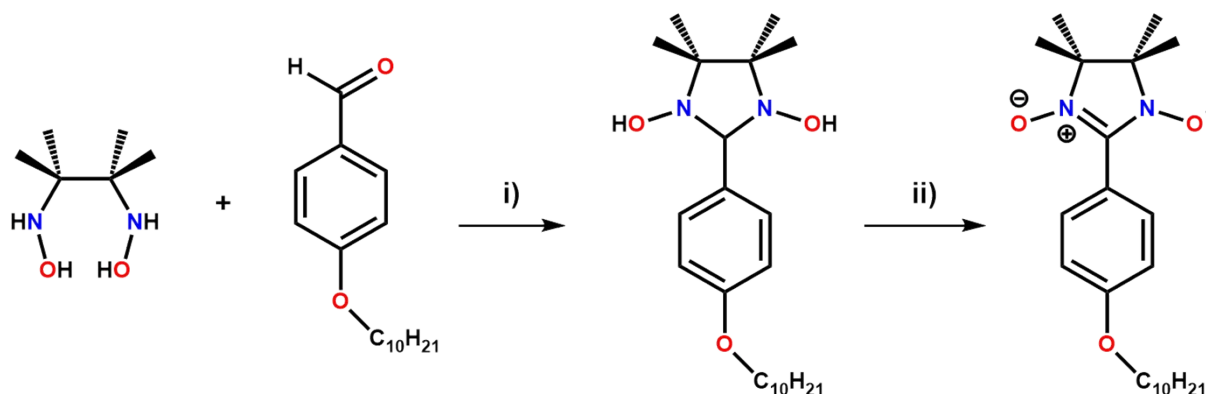2-(4'-(decyloxy)phenyl)-4,4,5,5-tetramethylimidazolin-1-oxyl-3-oxide

Figure S1. Synthetic pathway for the preparation of **NITPhOC10**: i) MeOH, 25°C, 24h; ii) NaIO$_4$, CH$_2$Cl$_2$:H$_2$O.

2.5 mmol (685 µL, 1 eq.) of commercially available 4-(decyloxy)benzaldehyde was added to 5 mmol (741 mg, 2 eq.) of Zn(2,3-bis(hydroxyamino)-2,3-dimethylbutane)Cl$_2$ in 50 mL of methanol, and stirred at room temperature for one day. The solution was dried and the remaining milky-white waxy solid was dissolved in 50 mL of cold CH$_2$Cl$_2$, then 50 mL of a NaIO$_4$ aqueous solution (641.6 mg, 3 mmol, 1.5 eq.) was added. The mixture immediately turned dark blue, the organic phase was washed several times with water (3 × 100 mL) and separated. The resultant organic solution was dried on Na$_2$SO$_4$, concentrated under reduced pressure and purified by flash silica gel (60-200 µm, 60 Å) column chromatography eluted with a 3/1 (*v/v*) ether/*n*-pentane solution. A dark blue fraction was collected and concentrated under reduced pressure, resulting of 350.6 mg (0.91 mmol) of fine blue crystalline solid. Yield: 36%. Single crystals suitable for single-crystal XRD were obtained by slow interdiffusion of 0.05 mmol (19.5 mg) of NITPhOC10 in 7 mL of CH$_2$Cl$_2$ layered with 10 mL of n heptane, kept at 4°C. Single crystals were isolated after few days. Elemental analysis (%) calcd. for C$_{23}$H$_{37}$N$_2$O$_3$: C 70.91; H 9.57; N 7.19. Found: C 71.37; H 9.59; N 7.29.

Syntheses of [Tb(hfac)$_3$(NITPhOCn)] (*n* = 6, 10, 18), "Pre-TbCn" powders
0.1 mmol (81.6 mg, 1eq.) of [Tb(hfac)$_3$·2H$_2$O] was dissolved in 40 mL of dry boiling *n*-heptane. The solution was concentrated until the volume reached 10 mL, then cooled to 75°C. 0.1 mmol of **NITPhOCn** (33.3, 38.9 and 50.1 mg for *n* = 6, 10, 18, resp.) dissolved in 3 mL of CHCl$_3$ was quickly added under stirring, and the obtained deep blue solution was then directly transferred to a 20 mL vial for immediate sonication. Pulsed sonication was performed with a Hielscher UP400 St sonicator using an S24d3 sonotrode (fixed frequency 24 kHz, diameter 3 mm) with a 90 % pulse rate (0.9 s of sonication/0.1 s of silence, ≈ 24 J per pulse) during 1 hour, for a total delivered energy of *E* = 86.4 kJ. The final mixture was dried under reduced pressure at room temperature, giving dark green powders for the TbC6 (yield: 59%) and TbC10 (yield: 60%), and a dark green latex-like solid for the TbC18 (yield: 65%). Elemental analysis (%) calcd. for TbC$_{34}$H$_{24}$N$_2$O$_9$F$_{18}$, TbC6): C 36.94; H 2.19; N 2.53. Found: C 36.94; H 2.93; N 2.65. Elemental analysis (%) calcd. for TbC$_{38}$H$_{40}$N$_2$O$_9$F$_{18}$, TbC10): C 39.02; H 3.45; N 2.40.

Found: C 39.18; H 3.44; N 2.36. Elemental analysis (%) calcd. for $TbC_{46}H_{56}N_2O_9F_{18}$, TbC18): C 43.10; H 4.40; N 2.19. Found: C 42.84; H 4.21; N 2.32.

Syntheses of [Tb(hfac)$_3$(NITPhOCn)$_2$] (n = 6, 10, 18) crystals, "TbCn monomers"

0.05 mmol (40.8 mg, 1eq.) of [Tb(hfac)$_3$·2H$_2$O] was dissolved in 40 mL of dry boiling n-heptane. The solution was concentrated until the volume reached 10 mL, then cooled to 75°C. 0.1 mmol of **NITPhOCn** (33.3, 38.9 and 50.1 mg for n = 6, 10, 18, resp.) dissolved in 3 mL of CHCl$_3$ was quickly added under stirring, and the obtained deep blue solution was allowed to cool at room temperature. The final solution was filtered and kept under evaporation at 4°C, giving dark red prisms after few days for the TbC6 (yield: 27%), TbC10 (yield: 32%) and TbC18 (yield: 20%).

Table S1. Crystallographic parameters of **NITPhOC10**.

M_w (g·mol^{-1})	389.54
Crystal system	Monoclinic
Space group	$P2_1/c$ (N°14)
a (Å)	8.4606(8)
b (Å)	31.157(3)
c (Å)	9.0987(9)
β (°)	111.456(4)
V (Å^3)	2232.3(4)
Z	4
T (K)	150(2)
2θ range	2.492 - 27.513 (25.021)
Reflns collected	9895
Indep. reflns	5088
Obs. reflns	4200
Parameters	253
$R_1{}^a$ ($I > 2\sigma(I)$) / $wR_2{}^b$ ($I > 2\sigma(I)$)	7.71 / 18.23

$$^a \sum(|F_0| - |F_c|)/\sum|F_0|$$

$$^b \sqrt{\sum w(|F_0|^2 - |F_c|^2)^2/\sum w(|F_0|^2)^2}$$

GOF	1.097
CCDC number	2298965
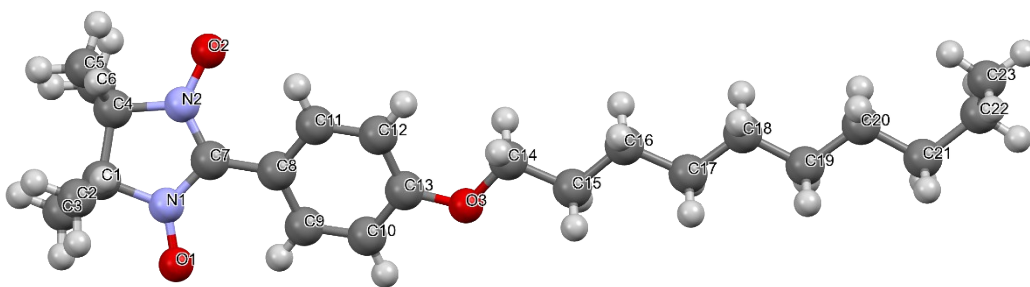
Figure S2. Molecular structure of **NITPhOC10**. Color code: red, O; blue, N; gray, C; white, H.
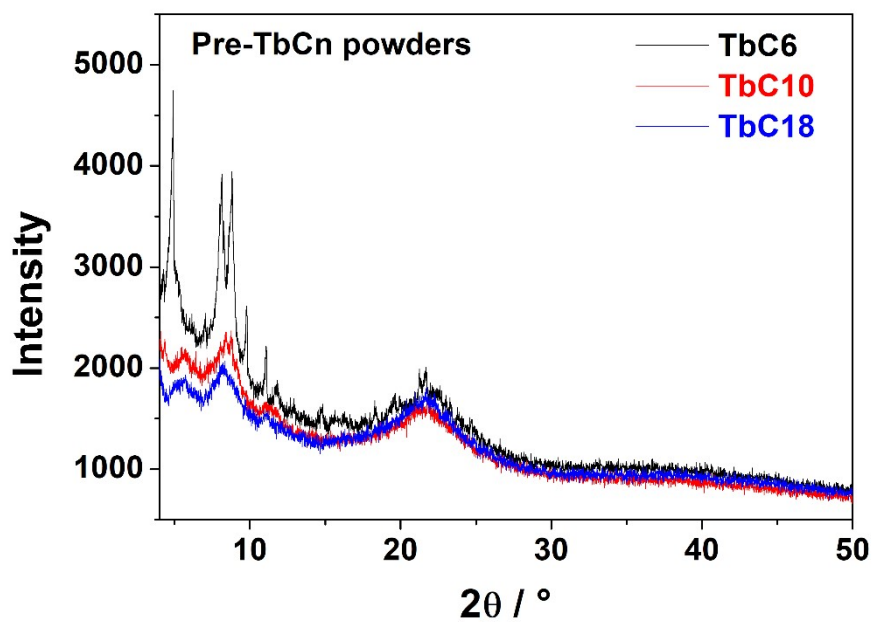
Figure S3. X-Ray Diffraction (XRD) diffractograms of **Pre-TbCn powders.**
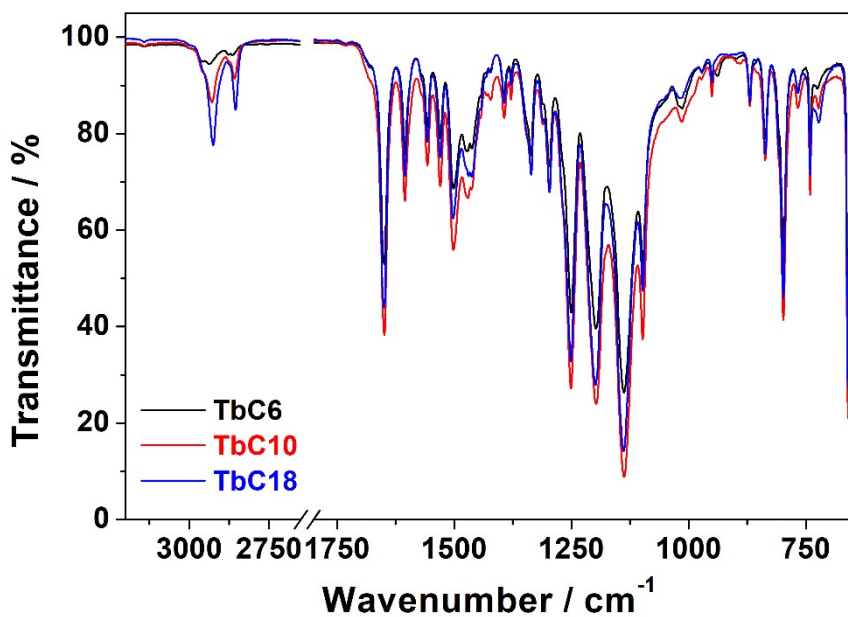
Figure S4. FT-IR spectra of **Pre-TbCn powders.**
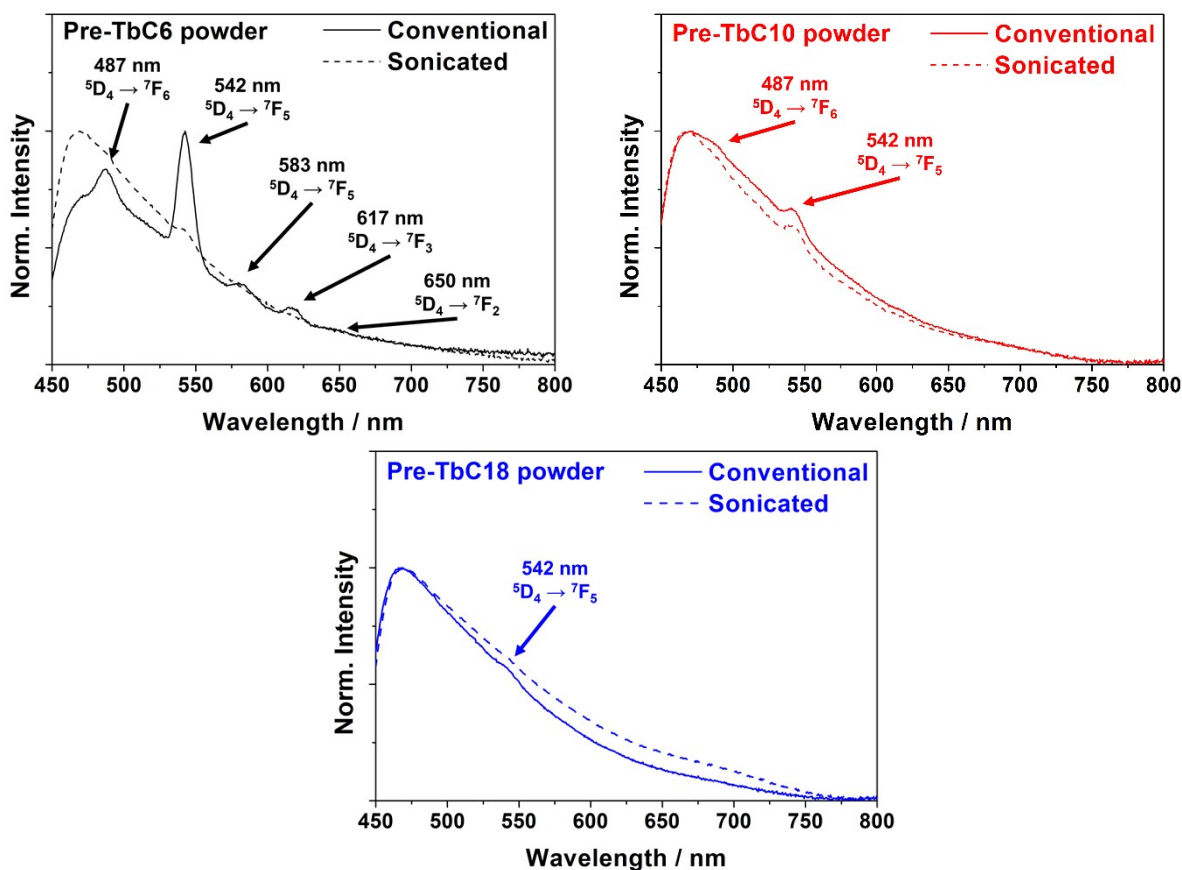
Figure S5. Solid-emission spectra (λ_{ex} = 300 nm) at 300 K of non-sonicated ("conventional") and "ultrasonicated" samples of **Pre-TbCn powders**.

Table S2. Minimum gelation concentration (C_{MG}) in mg·mL^{-1} of **TbCn gels** (S = Solution, I = Insoluble).

Solvent	TbC6	TbC10	TbC18
n-hexane	10	10	10
n-heptane	8	7	8
n-octane	8	6	8
n-decane	10	4	5
Cyclohexane	S	S	S
Xylenes, Toluene	S	S	S
Ether	S	S	S
Chloroform, DCM	S	S	S
Acetone, Acetonitrile	S	S	S
Methanol, Ethanol	S	S	S

| Water | I | I | I |
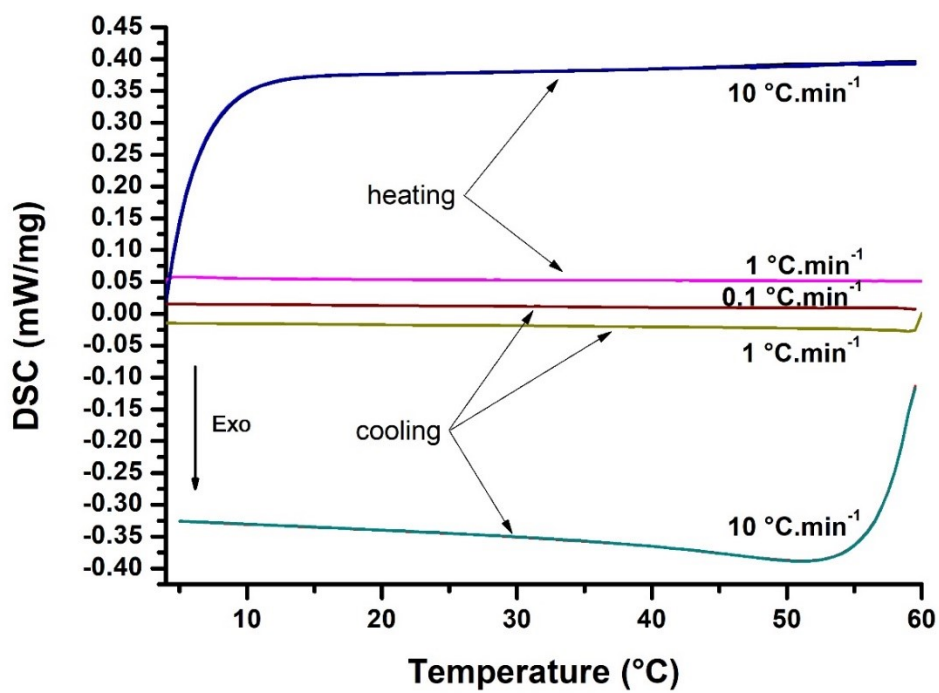
Figure S6. DSC traces of a *n*-heptane **TbC10 gel** (C_M = 10 mg·mL^{-1}) in sealed pan at different thermal scan rates).
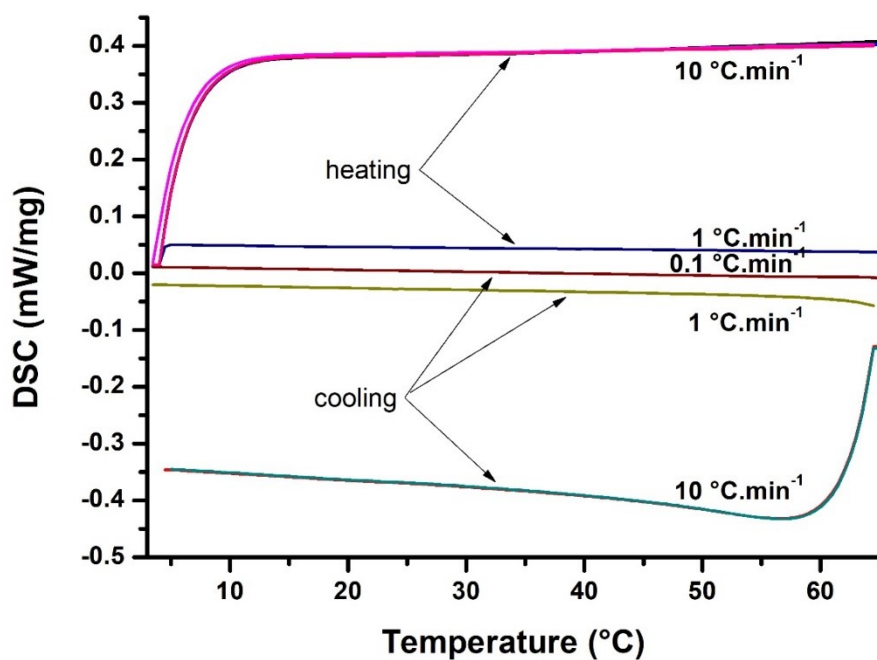
Figure S7. DSC traces of a *n*-heptane **TbC18 gel** (C_M = 10 mg·mL^{-1}) in sealed pan at different thermal scan rates).
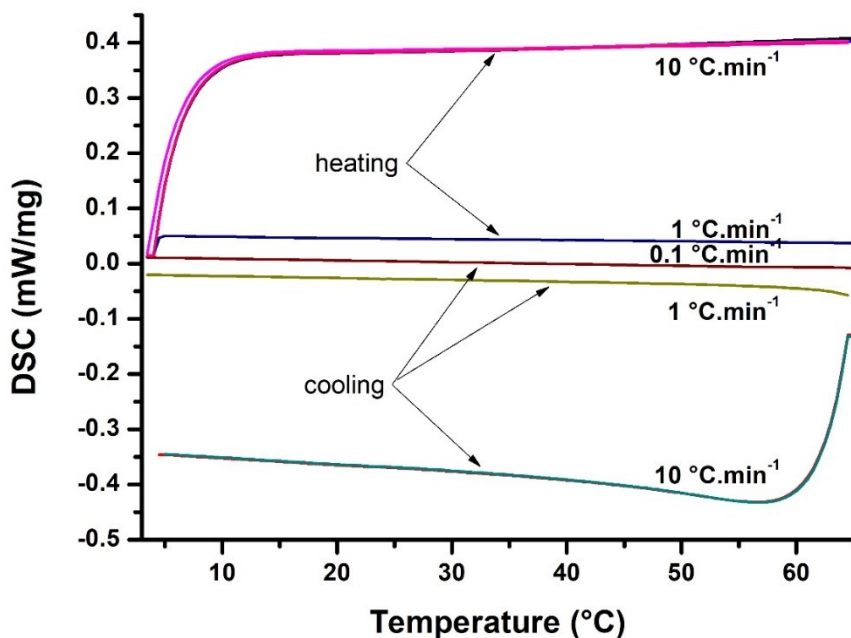
Figure S8. DSC curves of a *n*-heptane **TbC18 gel** (C_M = 50 mg·mL^{-1}) in sealed pan at different thermal scan rates).
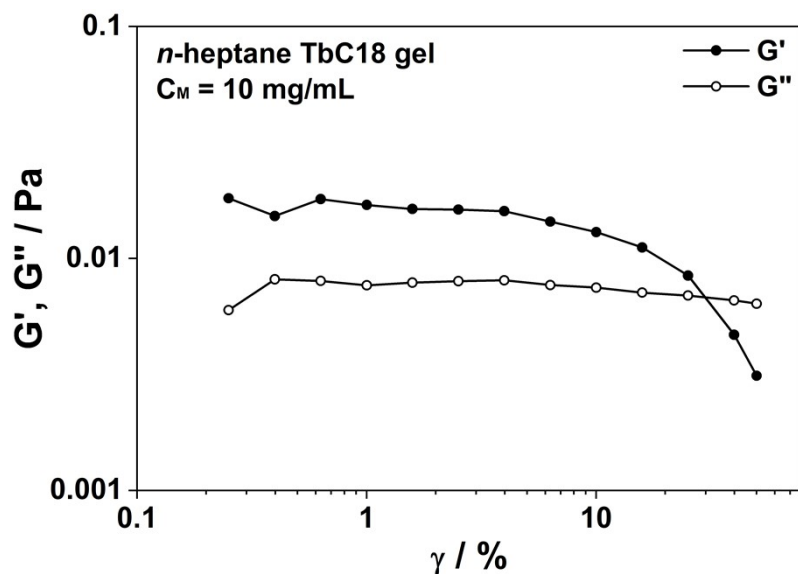
Figure S9. Oscillatory strain dependence of shear storage (*G'*) and loss (*G"*) modulus of **TbC18** gel (at 1 Hz frequency and *T* = 10°C).
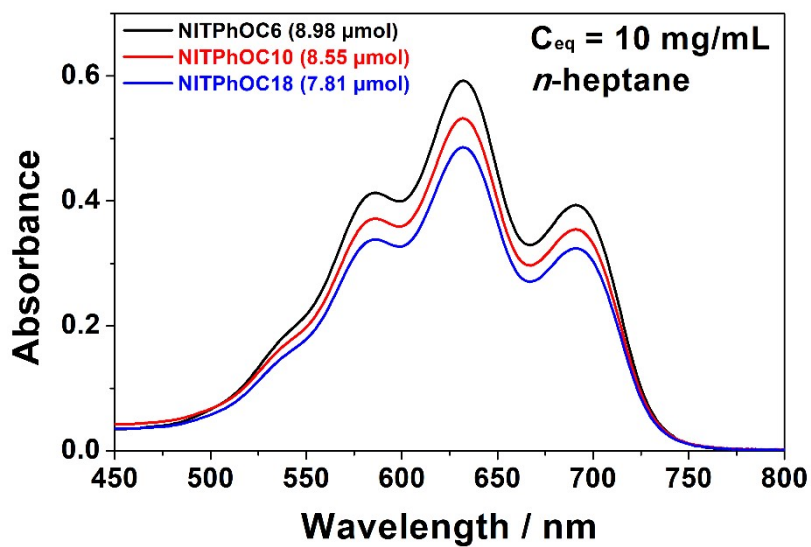
Figure S10. UV-visible spectrum of n-heptane **NITPhOPhCn** solutions (the different concentrations correspond to a mass concentration of C_M = 10 mg·mL^{-1} of the matching **TbCn gel**).
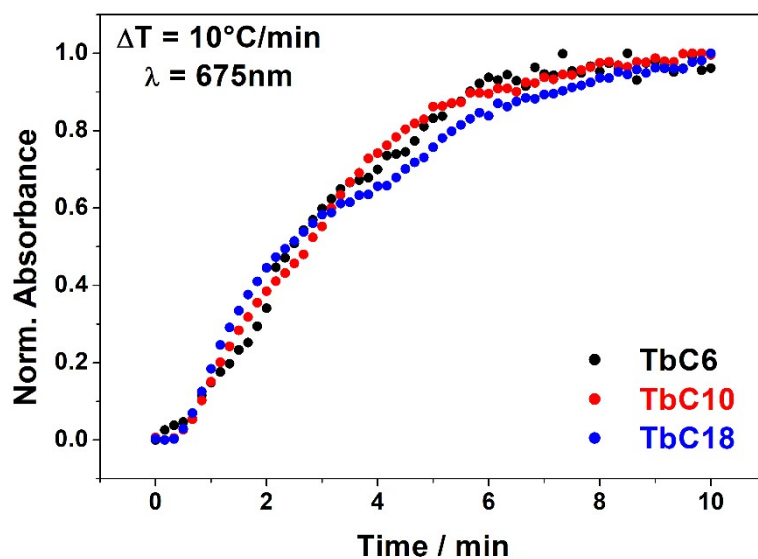
Figure S11. Time-resolved normalized absorbance of the *n*-heptane **TbCn gels** (C_M = 10 mg·mL^{-1}) at λ = 675 nm.
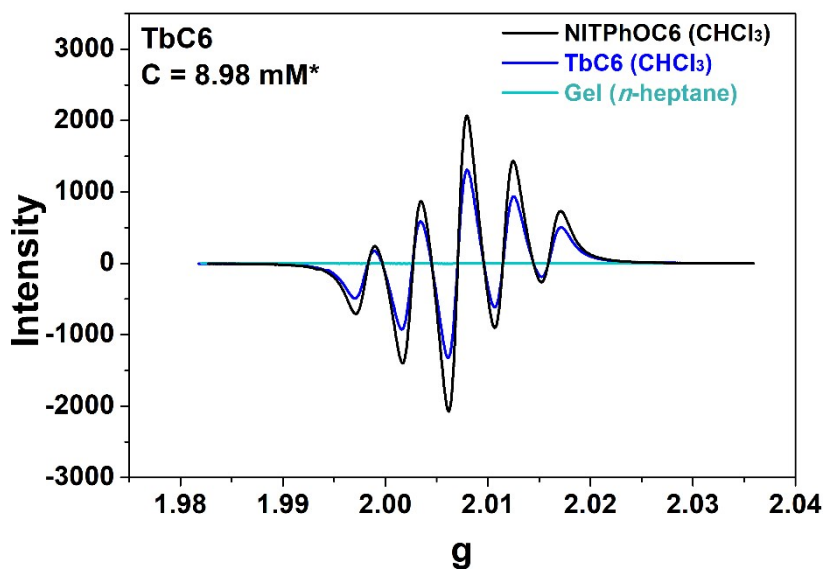
Figure S12. EPR X-band spectra of CHCl$_3$ solutions of **NITPhOC6** and **Pre-TbC6 powders**, and *n*-heptane **TbC6 gel** (*equivalent to C_M = 10 mg·mL^{-1} of TbC6 gel for comparison).
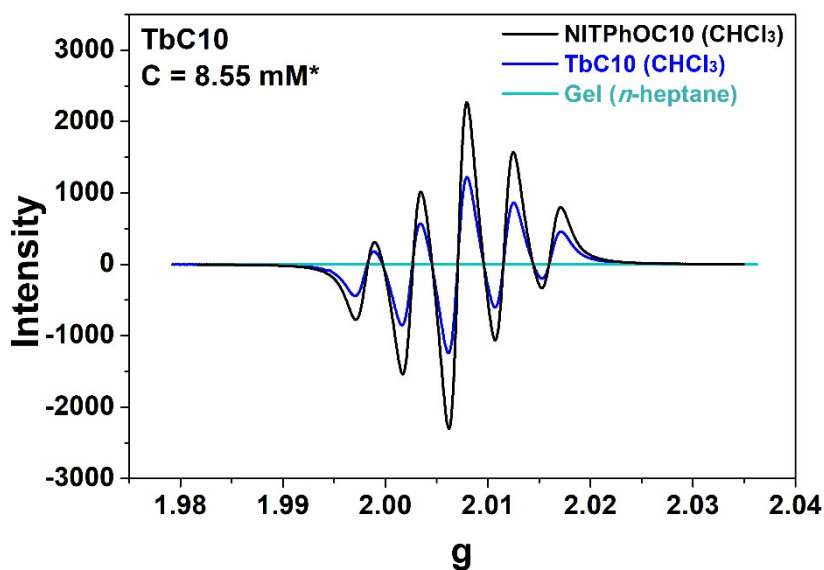
Figure S13. X-band EPR spectra of $CHCl_3$ solutions of **NITPhOC10** and **Pre-TbC10 powders**, and *n*-heptane **TbC10** gel (*equivalent to C_M = 10 mg·mL^{-1} of TbC6 gel for comparison).
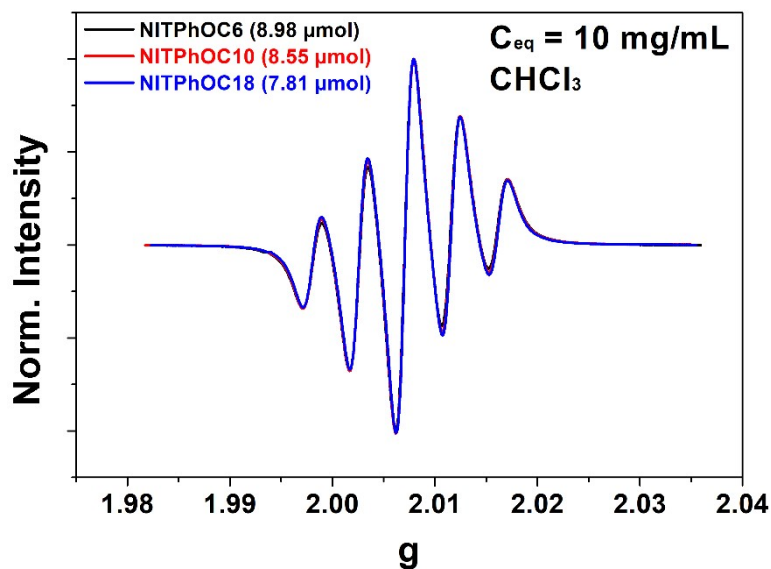
Figure S14. X-band EPR spectra of $CHCl_3$ solutions of **NITPhOCn** (*equivalent to a mass concentration C_M = 10 mg·mL^{-1} of TbCn compounds, resp. C = 8.98, 8.55 and 7.80 mM for **NITPhOC6**, **NITPhOC10** and **NITPhOC18**).
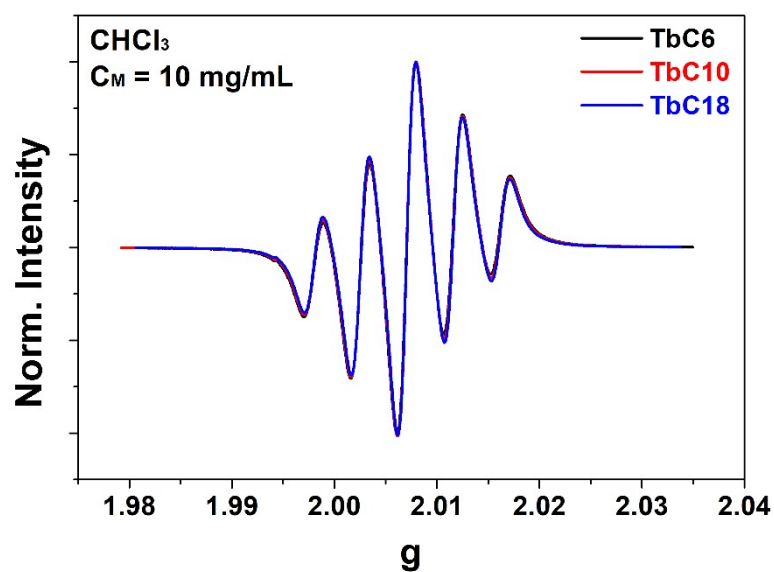
Figure S15. X-band EPR spectra of $CHCl_3$ solutions of **Pre-TbCn powders** (C_M = 10 mg·mL^{-1}).
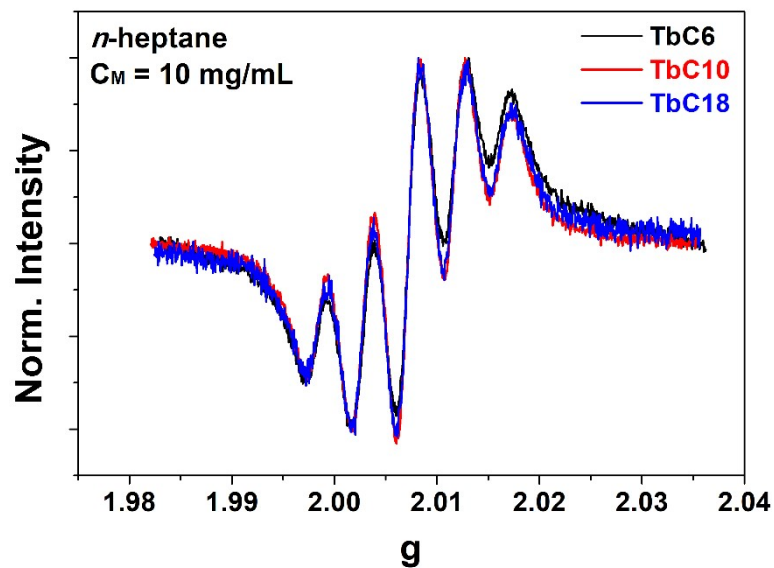
Figure S16. Zoom on the X-band EPR spectra of the *n*-heptane **TbCn gels** (C_M = 10 mg·mL^{-1}).

Table S3. EPR extracted g_e and hyperfine coupling a_n values for CHCl$_3$ solutions of **NITPhOCn** and **TbCn**, and *n*-heptane **TbCn gel**.

n	Solutions (CHCl$_3$)				Gels (*n*-heptane)	
	NITPhOC$_n$		TbC$_n$		TbC$_n$	
	g	a_n (mT)	*g*	a_n (mT)	*g*	a_n (mT)
6	2.0071	0.76	2.0070	0.77	2.0072	0.75
10	2.0071	0.76	2.0071	0.77	2.0072	0.75
18	2.0071	0.76	2.0071	0.77	2.0073	0.76

Magnetic properties
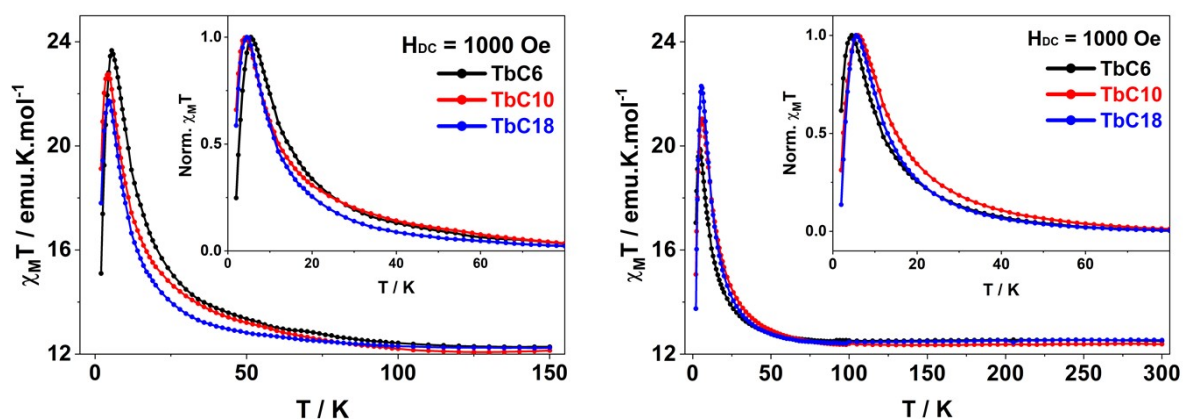
Figure S17. Temperature dependence of $\chi_M T$ measured with H_{DC} = 1000 Oe and with inset, a zoom in the low-temperature region of the normalised $\chi_M T$ of **TbCn gels** (left, C_M = 10 mg·mL^{-1}) and **Pre-TbCn powders** (right).
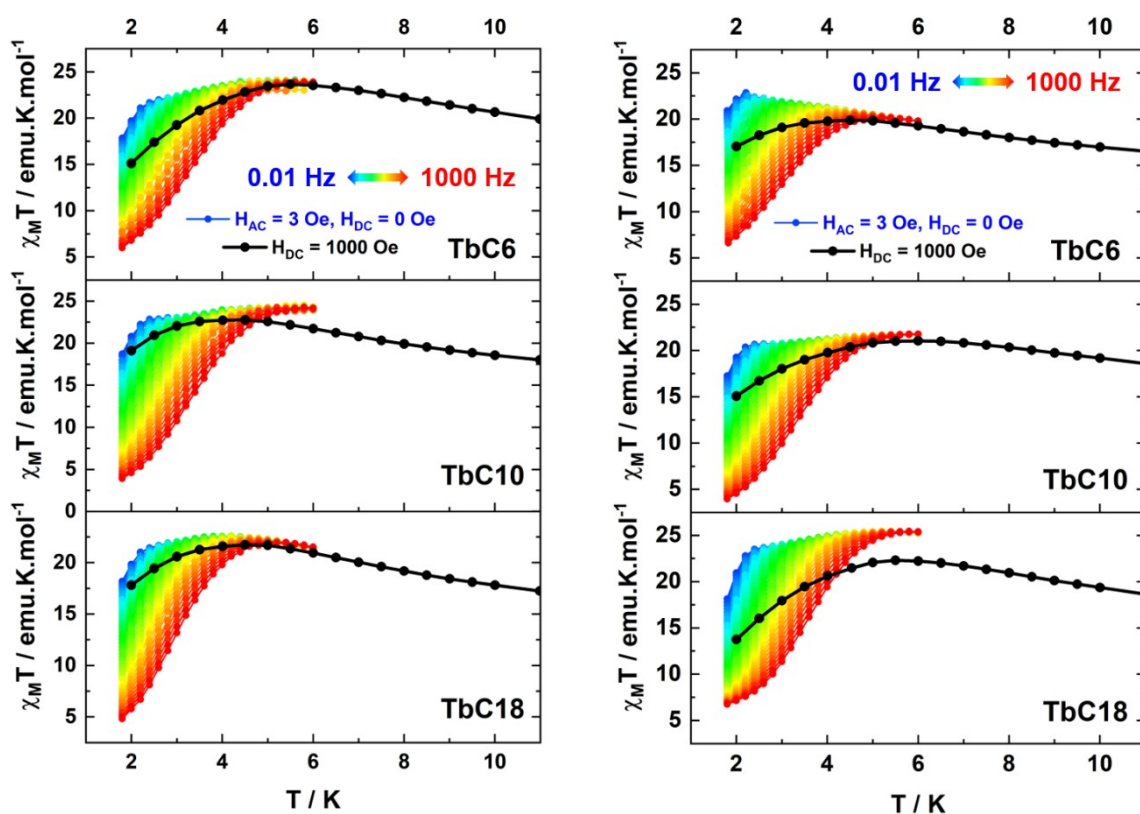

Figure S18. Temperature dependence of $\chi_M T$ measured with H_{DC} = 1000 Oe (black dots) and reconstructed from AC measurements with H_{AC} = 3 Oe (colour dots) at different frequencies for *n*-heptane **TbCn gels** (C_M = 10 mg·mL^{-1}) (left) and **Pre-TbCn powders** (right).
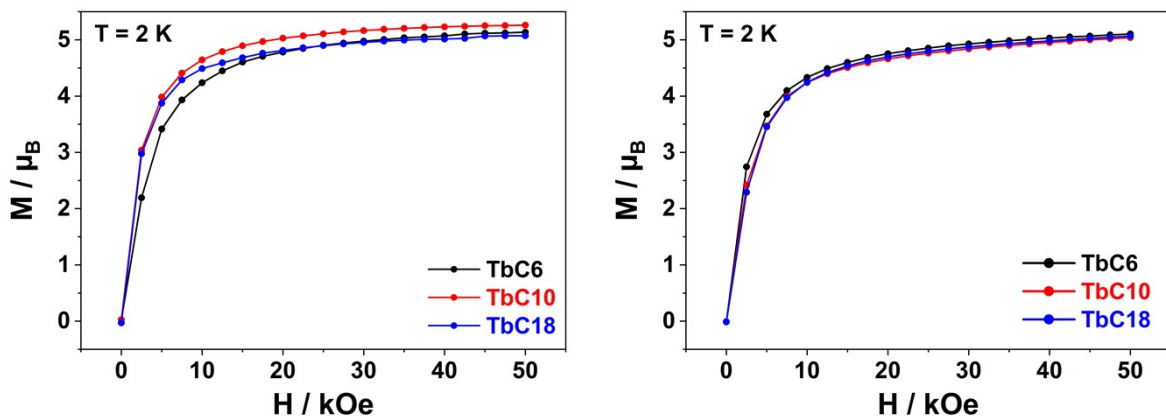
Figure S19. Field dependence of magnetisation of *n*-heptane **TbCn gels** (left, C_M = 10 mg·mL^{-1}) and **Pre-TbCn powders** (right).

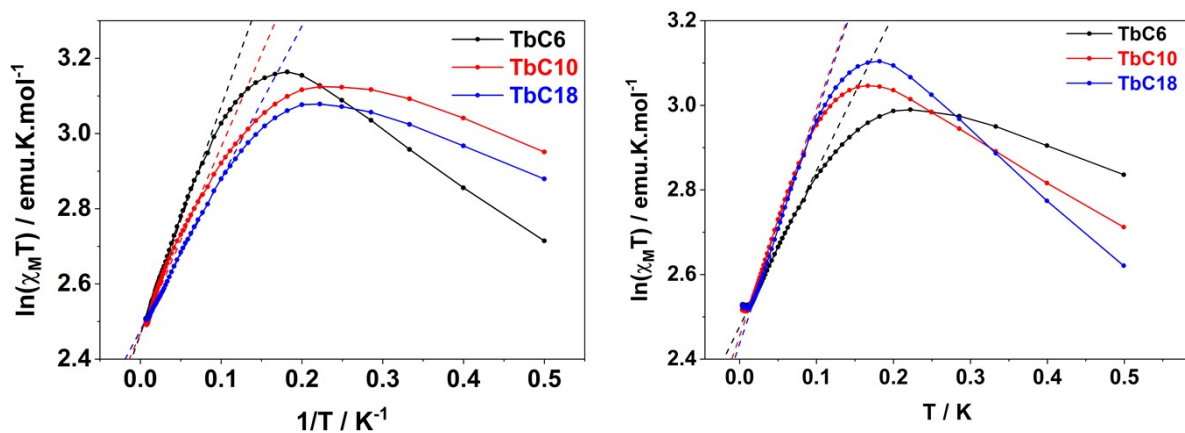**Figure S20.** Reciprocal temperature dependence of ln($\chi_M T$) measured with H_{DC} = 1000 Oe of **TbCn gels** (left, C_M = 10 mg·mL^{-1}) and **Pre-TbCn powders** (right).

Table S4. Characteristic values extracted from the temperature dependence of $\chi_M T$ of the **Pre-TbCn powders**.

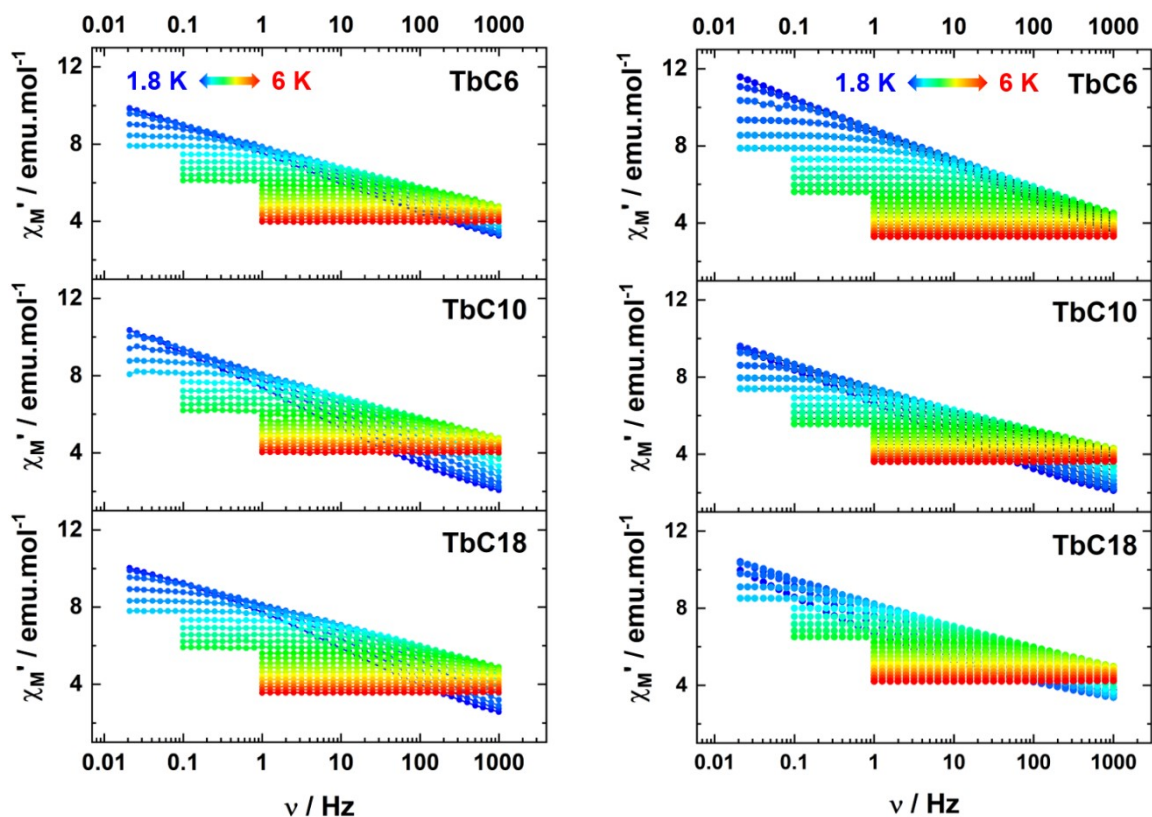|	C_{eff} (emu·K·mol^{-1})	$\Delta_{\xi(DC)}/k_B$ (K)
Pre-TbC6	11.90 ± 0.01	3.69 ± 0.02
Pre-TbC10	11.63 ± 0.02	5.36 ± 0.05
Pre-TbC18	11.43 ± 0.01	5.42 ± 0.03

Figure S21. Frequency dependency of the in-phase (χ_M') susceptibility of *n*-heptane **TbCn gels** (C_M = 10 mg·mL^{-1}, left) and **Pre-TbCn powders** (right) in zero external dc field at various temperatures.
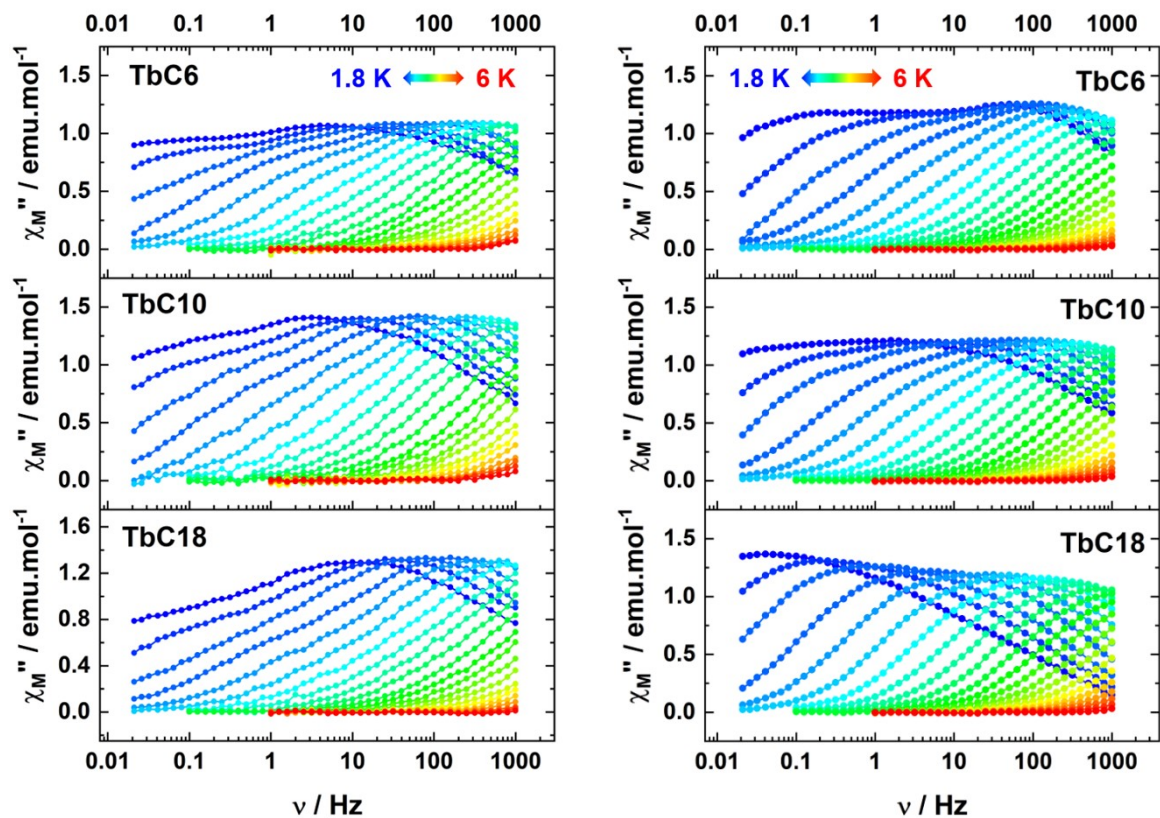

Figure S22. Frequency dependency of the out-of-phase (χ_M'') susceptibility of *n*-heptane **TbCn gels** (C_M = 10 mg·mL^{-1}, left) and **Pre-TbCn powders** (right) in zero external dc field at various temperatures.
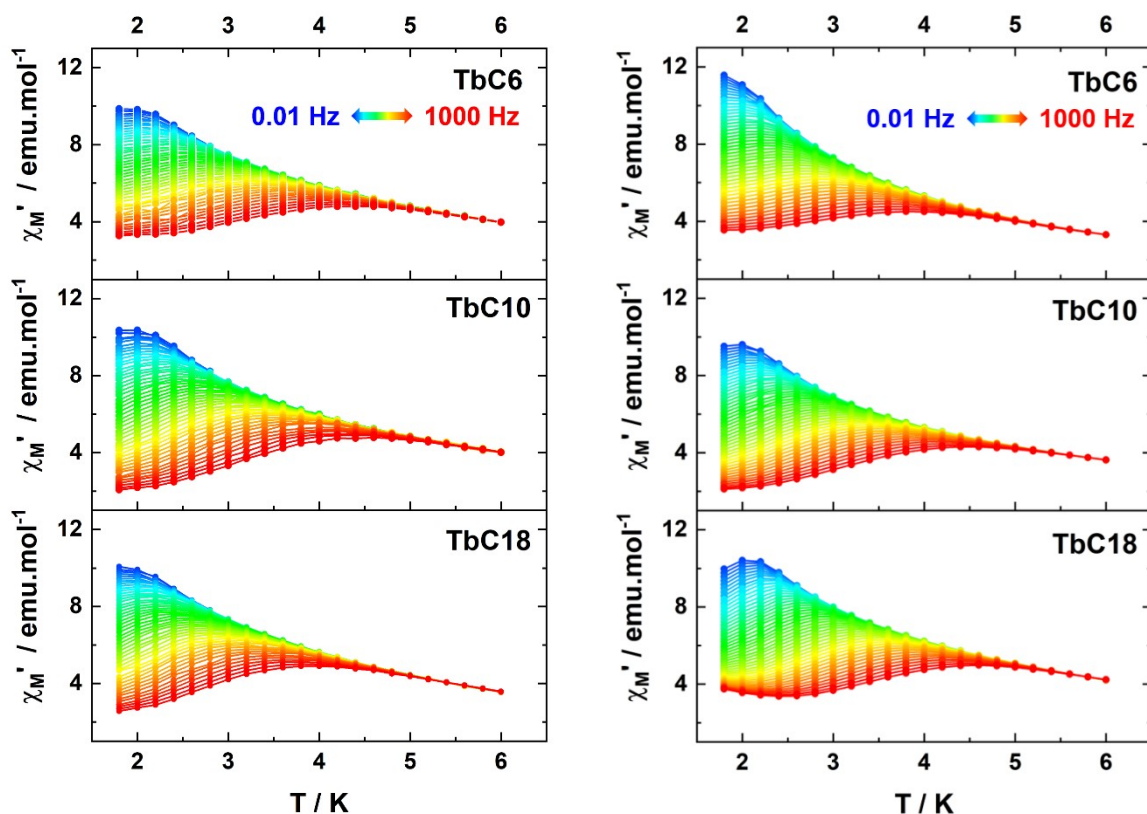
Figure S23. Temperature dependency of the in-phase (χ_M') susceptibility of *n*-heptane **TbCn gels** (C_M = 10 mg·mL^{-1}, left) and **Pre-TbCn powders** (right) in zero external dc field at various frequencies.

Figure S24. Temperature dependency of the out-of-phase (χ_M'') susceptibility of *n*-heptane **TbCn gels** (C_M = 10 mg·mL^{-1}, left) and **Pre-TbCn powders** (right) in zero external dc field at various frequencies.

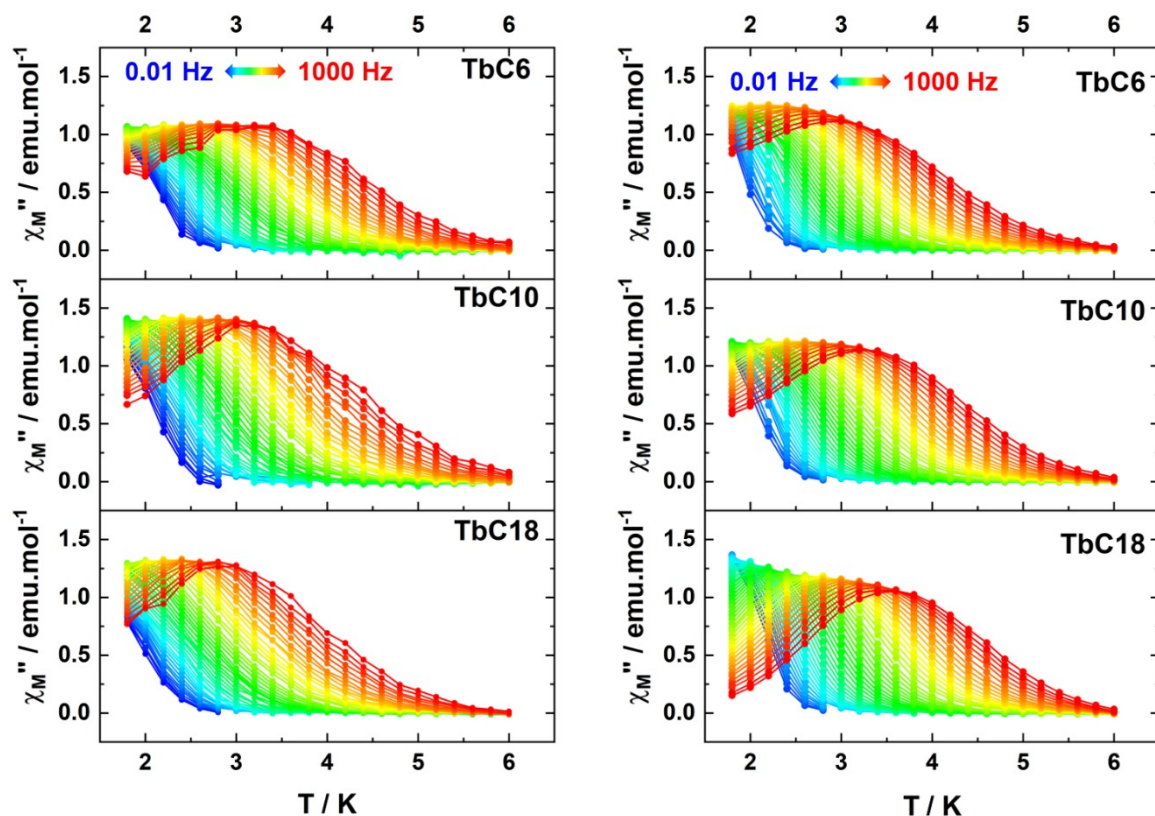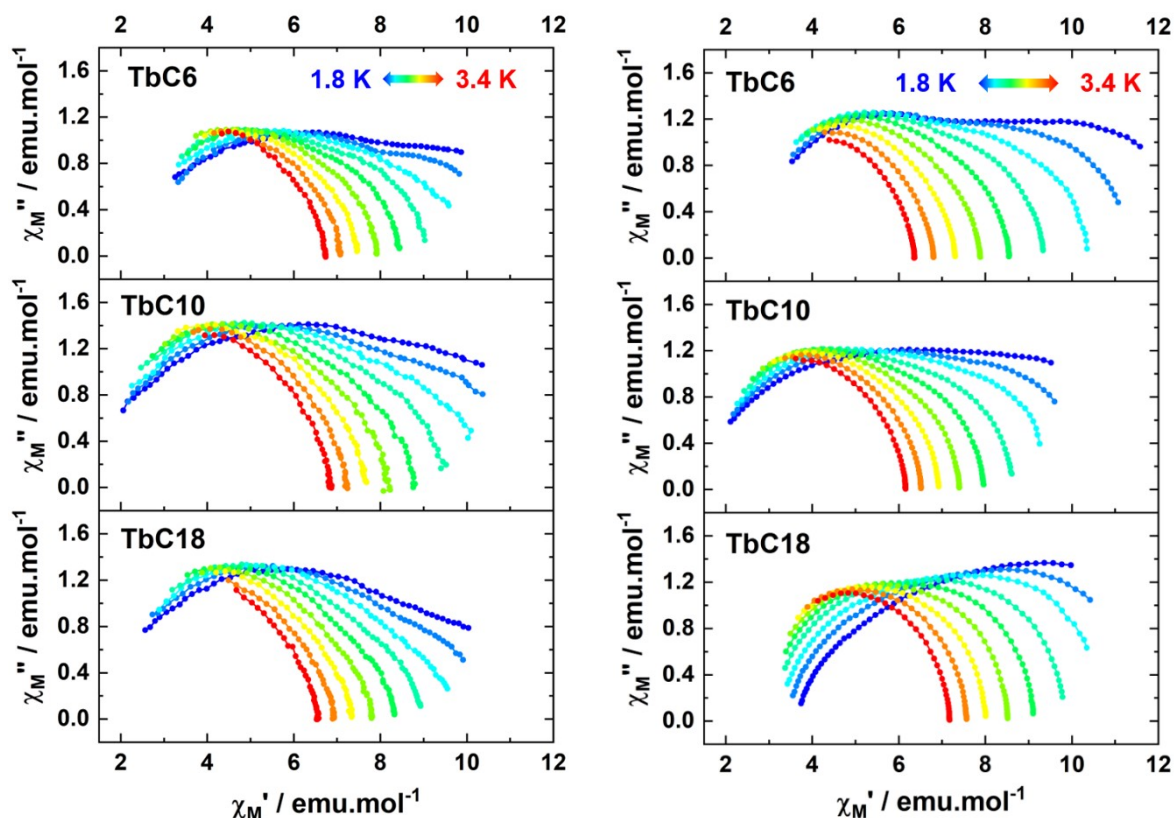**Figure S28.** Argand diagrams of *n*-heptane **TbCn gels** (C_M = 10 mg·mL^{-1}, left) and **Pre-TbCn powders** (right) in zero external dc field at various temperatures.

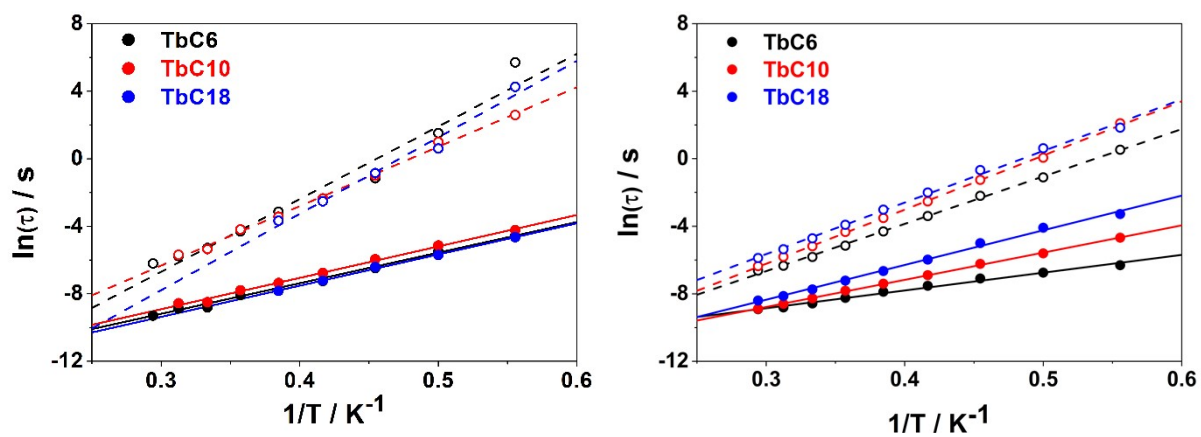**Figure S26.** Arrhenius plots of the extracted relaxation times with a double relaxation process for **TbCn gels** (left, C_M = 10 mg·mL^{-1}) and **Pre-TbCn powders** (right), with filled dots as fast mode and open circles as slow mode.

Table S5. Characteristic values extracted from the Arrhenius plots of the **Pre-TbCn powders** considering a double relaxation process.

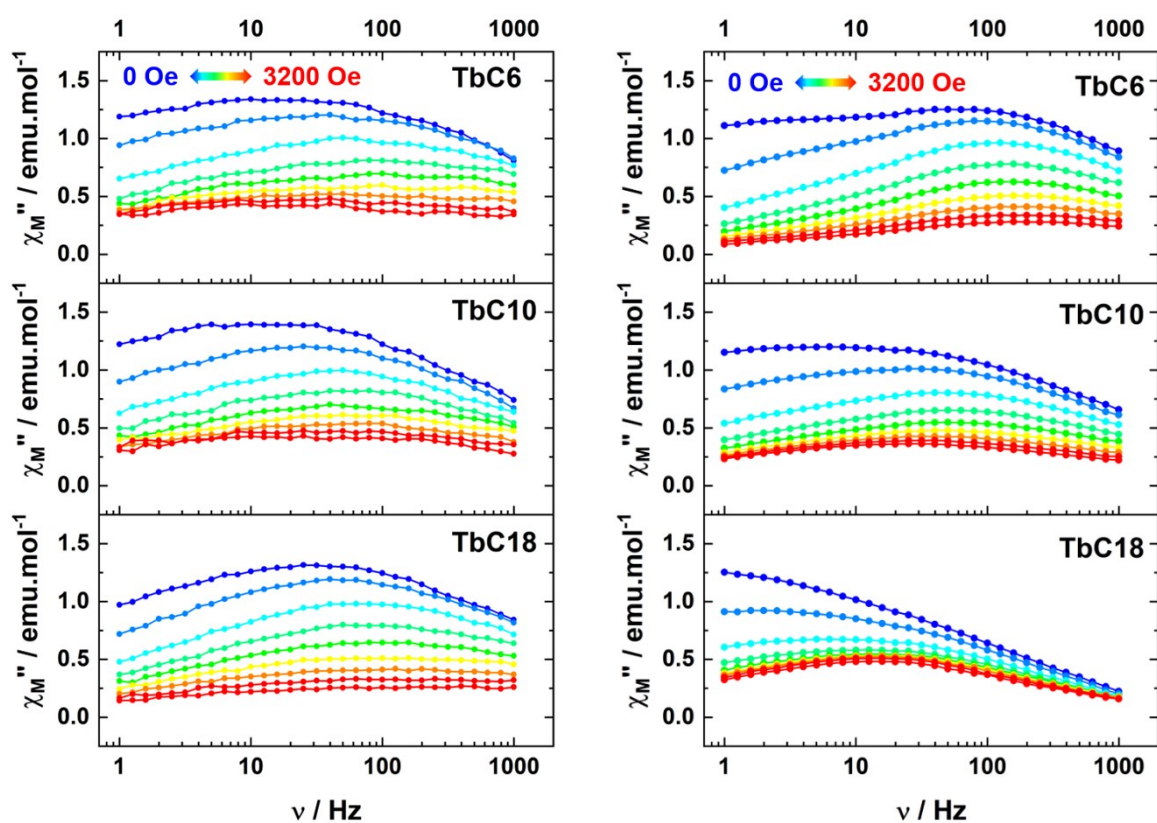|	TbC6		TbC10		TbC18	
	Slow	**Fast**	**Slow**	**Fast**	**Slow**	**Fast**
Δ_{eff}/k_B (K)	28.0 ± 0.4	10.5 ± 0.4	32.1 ± 0.3	16.1 ± 0.1	30.6 ± 0.7	20.5 ± 0.5
τ_0 (s)	(2.9 ± 0.5) x 10⁻⁷	(6.1 ± 1.0) x 10⁻⁶	(1.3 ± 0.2) x 10⁻⁷	(1.2 ± 0.1) x 10⁻⁷	(3.6 ± 1.2) x 10⁻⁷	(5.0 ± 1.1) x 10⁻⁷
R^2	0.9982	0.9890	0.9993	0.9993	0.9957	0.9956

Figure S27. Frequency dependency of the out-of-phase (χ_M'') susceptibility at 2 K of *n*-heptane **TbCn gels** (C_M = 10 mg·mL⁻¹, left) and **Pre-TbCn powders** (right) under various dc fields.
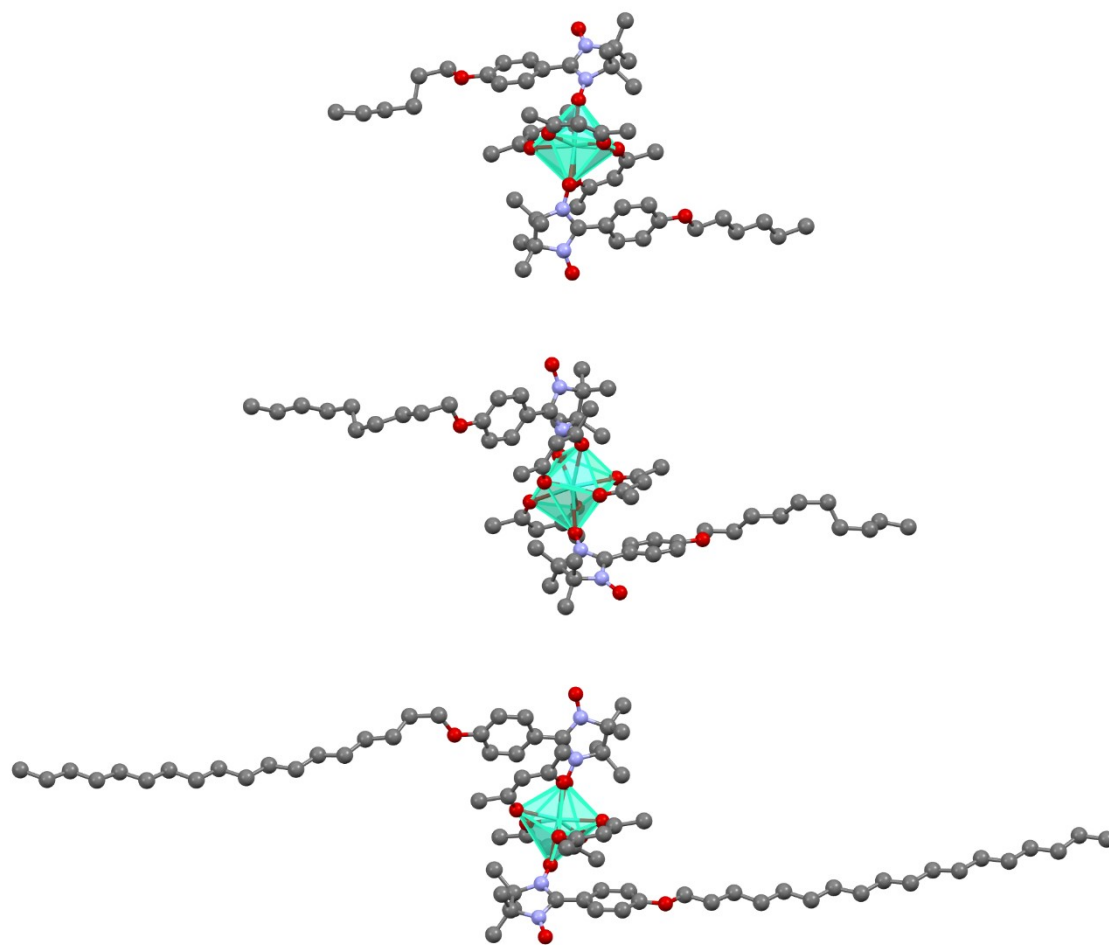
Figure S28. Molecular structures of **TbC6**, **TbC10** and **TbC18 monomers**. Color code: green, Tb; red, O; blue, N; gray, C. Fluorine and hydrogen atoms have been omitted for clarity.

Table S6. Crystallographic parameters of **TbCn monomers**.

	[Tb(hfac)₃(NITPhOC6)₂]	[Tb(hfac)₃(NITPhOC10)₂]	[Tb(hfac)₃(NITPhOC18)₂]
M_w (g·mol^{-1})	1446.97	1559.18	1783.60
Crystal system	Triclinic	Triclinic	Triclinic
Space group	P-1 (N°2)	P-1 (N°2)	P-1 (N°2)
a (Å)	12.2458(11)	12.1275(6)	12.1749(13)
b (Å)	16.2452(16)	16.4424(8)	19.0492(19)
c (Å)	19.1763(17)	19.0044(10)	19.101(2)
α (°)	75.757(3)	109.560(2)	82.310(4)
β (°)	81.276(3)	99.282(2)	76.509(4)
γ (°)	70.425(4)	96.610(2)	81.629(4)
V (Å³)	3473.8(6)	3465.4(3)	4238.8(8)
Z	2	2	2
T (K)	150(2)	150(2)	150(2)
2θ range	1.868 - 27.488 (25.620)	2.235 - 27.517 (25.282)	1.933 - 27.521 (25.588)
Reflns collected	50521	39870	66658
Indep. reflns	15866	15716	19411
Obs. reflns	14586	14173	17136
Parameters	775	860	958
R_1 ($I > 2\sigma(I)$)	3.47	4.03	3.83
wR_2 ($I > 2\sigma(I)$)	8.79	10.11	9.92
GOF	1.086	1.145	1.241
CCDC number	2298968	2298966	2298967

Table S7. Continuous Shape Measurements (CShM)[6] for **TbCn monomers**.

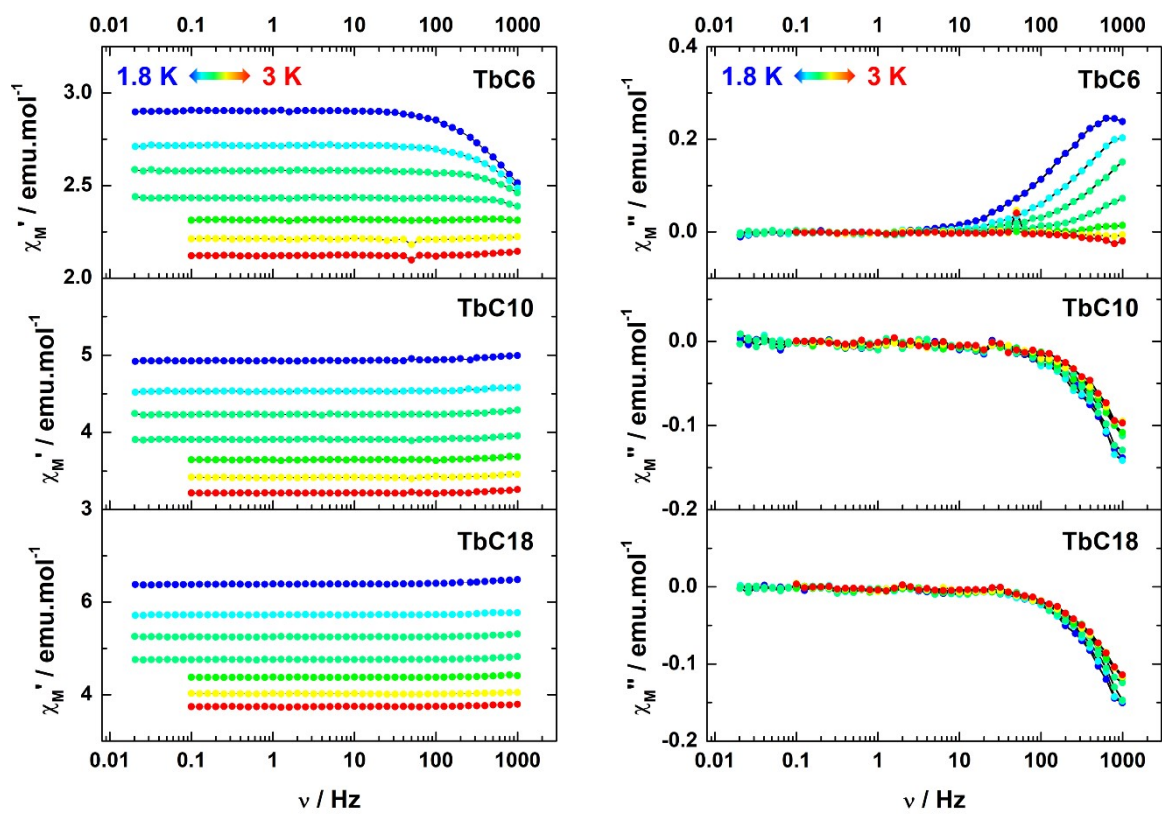| Coordination geometry (site symmetry)	Square antiprism (D_{4d})	Triangular dodecahedron (D_{2d})	Bi-augmented trigonal prism (C_{2v})
[Tb(hfac)₃(NITPhOC6)₂]	1.602	**0.252**	1.916
[Tb(hfac)₃(NITPhOC10)₂]	1.356	**0.480**	1.537
[Tb(hfac)₃(NITPhOC18)₂]	1.842	**0.201**	1.853

Figure S29. Frequency dependency of the in-phase (χ_M', left) and out-of-phase (χ_M'', right) susceptibilities of grounded microcrystalline powders of **TbCn monomers** in zero external dc field at various temperatures.
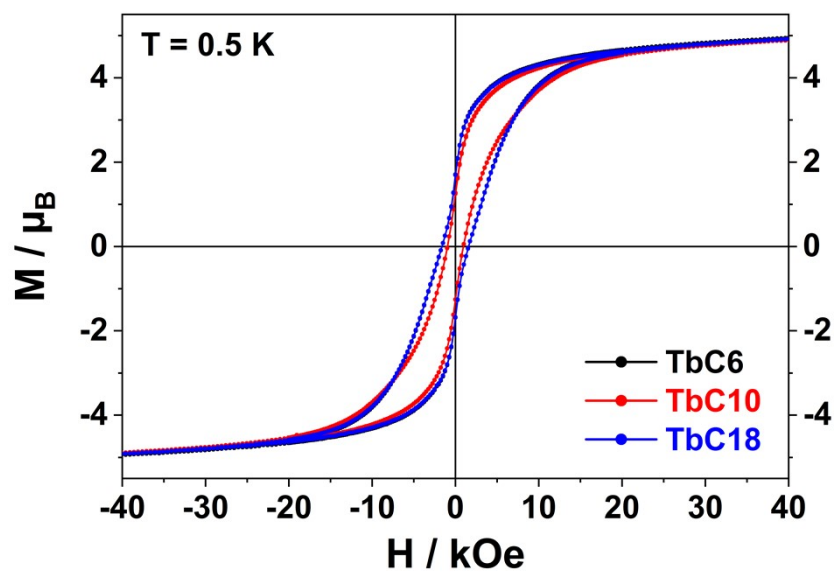
Figure S30. Magnetic hysteresis curves of **Pre-TbCn powders** measured at 0.5 K ($\Delta H/\Delta t$ = 15.5 Oe·s^{-1}).

Table S8. Coercive fields HC and remanent magnetisations MR reported for the *n*-heptane **TbCn gels** (C_M = 10 mg·mL^{-1}) and **Pre-TbCn powders** at 0.5 K.

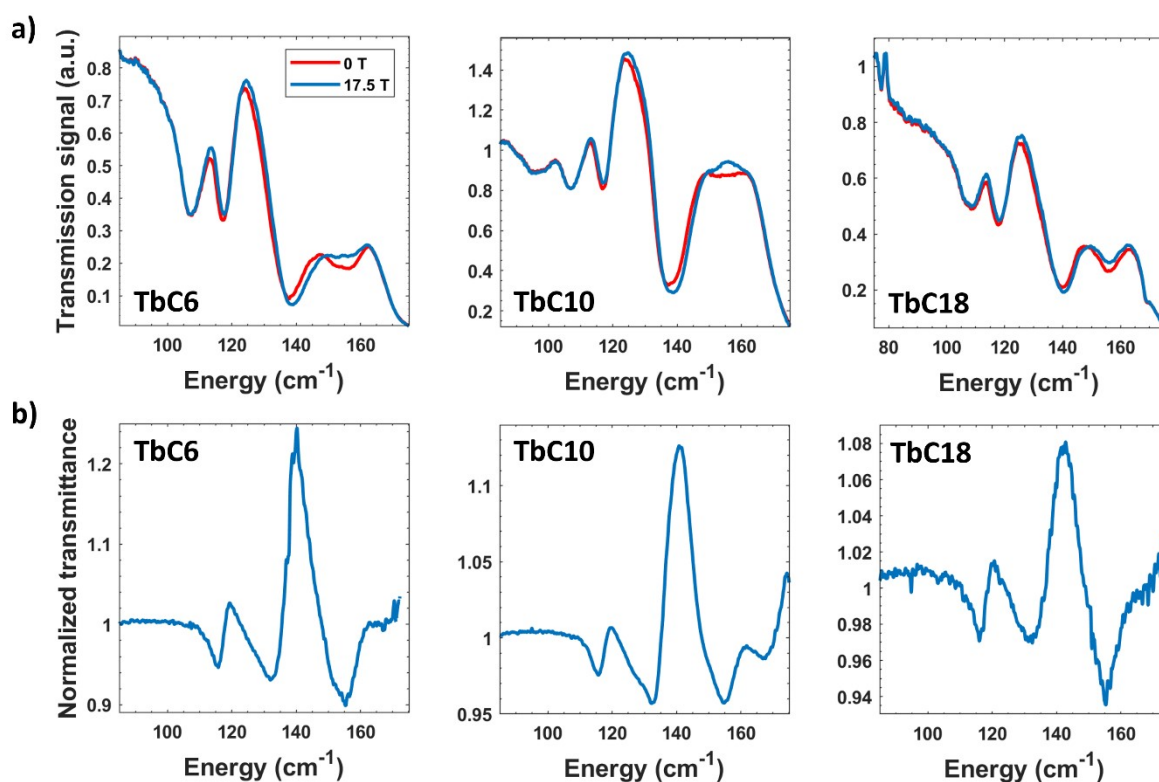|		H_C (Oe)	M_R (μ_B) / %M$_{sat}$
TbC$_6$	**Gel**	3440	2.49 / 50 %
	Precursor	1600	1.70 / 34 %
TbC$_{10}$	**Gel**	2780	2.23 / 45 %
	Precursor	1000	1.27 / 26 %
TbC$_{18}$	**Gel**	1610	1.94 / 39 %
	Precursor	1600	1.71 / 34 %

Figure S31. Low-temperature far-infrared data measured for **TbC6** (left), **TbC10** (middle) and **TbC18** (right) xerogels. The energy axes margins are chosen within the spectra range exhibiting the largest magnetic response. The top panel (a) shows the single-beam spectrum of the transmitted IR intensity measured at two different magnetic fields. The low-energy part is indifferent to the magnetic field, whereas noticeable changes of the same nature occur in the vicinity of 115, 131, and 155 cm^{-1}. The bottom panel (b) shows the normalized transmittance spectrum at the zero magnetic field, which is equivalent to the zero-field cut of the FIRMS heatmap plotted in the main text.

References

1. Sheldrick, G. M. *SHELXT* – Integrated space-group and crystal-structure determination. *Acta Crystallogr. Sect. Found. Adv.* **71**, 3–8 (2015).
2. Sheldrick, G. M. Crystal structure refinement with *SHELXL*. *Acta Crystallogr. Sect. C Struct. Chem.* **71**, 3–8 (2015).
3. Farrugia, L. J. *WinGX* and *ORTEP for Windows* : an update. *J. Appl. Crystallogr.* **45**, 849–854 (2012).
4. Bizien, T., Ameline, J.-C., Yager, K. G., Marchi, V. & Artzner, F. Self-Organization of Quantum Rods Induced by Lipid Membrane Corrugations. *Langmuir* **31**, 12148–12154 (2015).
5. Nečas, D. & Klapetek, P. Gwyddion: an open-source software for SPM data analysis. *Open Phys.* **10**, 181–188 (2012).
6. Llunell, M., Casanova, D., Cirera, J., Alemany, P. & Alvarez, S. SHAPE. (2010).